

UNVEILING A POPULATION OF X-RAY NON-DETECTED AGN

J. L. DONLEY,¹ G. H. RIEKE,¹ J. R. RIGBY,¹ P. G. PÉREZ-GONZÁLEZ¹

Accepted for publication in The Astrophysical Journal

ABSTRACT

We define a sample of 27 radio-excess AGN in the *Chandra* Deep Field North by selecting galaxies that do not obey the radio/infrared correlation for radio-quiet AGN and star-forming galaxies. Approximately 60% of these radio-excess AGN are X-ray undetected in the 2 Ms *Chandra* catalog, even at exposures of ≥ 1 Ms; 25% lack even 2σ X-ray detections. The absorbing columns to the faint X-ray-detected objects are $10^{22} \text{ cm}^{-2} < N_{\text{H}} < 10^{24} \text{ cm}^{-2}$, i.e., they are obscured but unlikely to be Compton thick. Using a local sample of radio-selected AGN, we show that a low ratio of X-ray to radio emission, as seen in the X-ray weakly- and non-detected samples, is correlated with the viewing angle of the central engine, and therefore with obscuration. Our technique can explore the proportion of obscured AGN in the distant Universe; the results reported here for radio-excess objects are consistent with but at the low end of the overall theoretical predictions for Compton-thick objects.

Subject headings: galaxies: active — X-rays: galaxies — radio continuum: galaxies

1. INTRODUCTION

Hard X-ray surveys are an efficient means to define AGN samples, as hard X-ray emission is able to penetrate the dust and gas capable of obscuring an AGN's optical, UV, and soft X-ray emission. However, AGN with high columns of absorbing gas can be missed even in the hard (2-10 keV) X-ray. Many local AGN have very high absorbing column; Seyfert 2's are about four times more numerous than Seyfert 1s (Maiolino & Rieke 1995), and more than half of Seyfert 2 nuclei are Compton thick with $N_{\text{H}} > 10^{24} \text{ cm}^{-2}$ (Maiolino et al. 1998; Risalti et al. 1999). X-ray background population synthesis models predict that AGN are similarly obscured out to high ($z = 2 - 3$) redshift; $\sim 60\%$ of high-redshift AGN are predicted to have obscuring columns greater than $N_{\text{H}} = 10^{23} \text{ cm}^{-2}$ (e.g., Comastri et al. 2001, Gilli 2004). If distant AGN are indeed this obscured, the deep hard X-ray *Chandra* surveys will be moderately incomplete for obscured AGN ($N_{\text{H}} > 10^{22} \text{ cm}^{-2}$); Treister et al. (2004) estimate 25% incompleteness at $N_{\text{H}} = 3 \times 10^{23} \text{ cm}^{-2}$. Such surveys will also miss nearly all of the Compton-thick AGN, a large population of which are expected both locally and in the high-redshift Universe (c.f. Ueda et al. 2003).

Quantifying the fraction of AGN missed by current surveys is necessary if we are to understand the accretion history of the Universe. In addition, the identification of heavily obscured AGN is in itself interesting, as such sources are poorly understood in the distant Universe.

The availability of deep mid-infrared (MIR) and radio images of the *Chandra* Deep Field North (CDFN) provides a new way to search for heavily obscured AGN, as extinction in the MIR and radio is small. Radio-excess AGN are significantly brighter in the radio relative to the infrared than are star-forming galaxies, which fit the well-defined radio/infrared correlation (Helou et al. 1985; Appleton et al. 2004). With the deep MIR data, we have separated the radio-excess AGN population from star-forming galaxies by comparing their radio and MIR flux densities. Because this radio/infrared method of classification is independent of the optical, UV, and X-ray characteristics of the deep radio sample,

we detect via this selection approach AGN that are missed at other wavelengths, thereby testing the completeness of current AGN samples. We find that a significant number of radio-excess AGN do not appear even in the deepest available X-ray surveys.

This paper is organized as follows. In §2 we discuss the radio and infrared observations and data reduction. The X-ray faint AGN population is introduced in §3, followed by a discussion of redshifts in §4. We focus in §5 on lower-significance X-ray detections, along with the X-ray coaddition of undetected AGN. The discussion follows in §6, and we summarize the conclusions of the paper in §7.

2. OBSERVATIONS AND DATA REDUCTION

Our initial sample consists of 371 radio sources detected at 1.4 GHz by the Richards et al. (2000) VLA survey of the CDFN; this survey has a detection limit of $40 \mu\text{Jy}$, rms noise of $\sim 7.5 \mu\text{Jy}$, and is 95% complete to $80 \mu\text{Jy}^2$. We later restrict this initial sample to those sources with X-ray exposures > 1 Ms; this reduces the radio sample size to 162, and the effective area of the survey to $\sim 230 \text{ arcmin}^2$ (Alexander et al. 2003).

The $24 \mu\text{m}$ properties of the radio sources are determined from a $\sim 1400\text{s}$ Spitzer MIPS observation of the CDFN. The MIPS $24 \mu\text{m}$ image was processed with the MIPS GTO data analysis tool (Gordon et al. 2004). The measured count rates are corrected for dark current, cosmic-rays, and flux nonlinearities, and are then divided by flat-fields for each MIPS scan-mirror position. Images are then interpolated to half pixels, corrected for geometric distortion, and mosaicked. The final mosaic has a pixel scale of $1''.25 \text{ pix}^{-1}$, with a point-spread function full-width at half maximum (FWHM) of $\approx 6''$. Source extraction at $24 \mu\text{m}$ was performed using the task *allstar* in the DAOPHOT package of IRAF³ (see Pérez-González et al. 2005). We detect 1868 $24 \mu\text{m}$ sources in the

² A rereduction of the radio data by G. Morrison shows flux density differences from the original reduction that are generally no more than $\sim 10\%$, with the notable exception of source VLA J123659+621832, where there is a discrepancy by a factor of ten (private communication, F. Bauer and G. Morrison). Adopting the new value for this source would push it further into the AGN regime in our selection method but would have no effect on the conclusions of this paper.

³ IRAF is distributed by the National Optical Astronomy Observatories,

¹ Steward Observatory, University of Arizona, 933 North Cherry Avenue, Tucson, AZ 85721; jdonley@as.arizona.edu

> 1 Ms field, 1167 of which have flux densities higher than the 80% completeness limit of the MIPS $24 \mu\text{m}$ image processed in this manner, $80 \mu\text{Jy}$ (Papovich et al. 2004). Systematic photometric errors in the MIPS photometry are small ($\sim 1\%$), so the measurement accuracy is determined by statistical errors (about $15 \mu\text{Jy rms}$) and confusion noise (about $11 \mu\text{Jy rms}$).

The 1.4 GHz and $24 \mu\text{m}$ sources were matched using a $2''$ search radius, after adjusting the $24 \mu\text{m}$ positions to remove any systematic positional offset between the radio and infrared images. We exclude from our final radio-excess AGN sample one radio source whose nearest $24 \mu\text{m}$ counterpart lies between $2''$ and $3''$ of the radio position, as the reliability of counterparts in this region is ambiguous. If a source was not detected because it is blended with a brighter $24 \mu\text{m}$ source, we use the flux density of the blended source as a conservative upper limit. Sources that were not detected at $24 \mu\text{m}$ were assigned the $\sim 5\sigma$ limit of $80 \mu\text{Jy}$. At the detection limits, there are ~ 0.7 radio sources and ~ 5 infrared sources per square arcmin. Consequently, one expects ~ 3 false coincidences of radio and $24 \mu\text{m}$ sources in the entire sample. Since we identify AGN by their relatively faint $24 \mu\text{m}$ flux densities, the false detections will tend to remove some AGN from our sample but will not bias our results otherwise.

We also use a 500 s IRAC observation of the CDFN. The IRAC observations were divided into 4 dithers of 125 s each; the 5σ point source sensitivity limits for the IRAC 3.0, 4.5, 5.8, and $8.0 \mu\text{m}$ bands are 1.4, 2.8, 18.4, and $22.7 \mu\text{Jy}$ respectively (Fazio et al. 2004). The IRAC data analysis is described in Huang et al. (2004). Source extraction in the IRAC bands was conducted using SExtractor (Bertin & Arnouts 1996).

Optical and near-infrared (NIR) photometry are measured from datasets published for the CDFN by the GOODS team (*bviz*, Giavalisco et al. 2004) and by Capak et al. (2004) (*UB-VRIzHK*). When there is a single optical counterpart within $2''$ of the radio source, the optical and NIR magnitudes are aperture-matched for consistency as described in Pérez-González et al. (2005). For radio sources with more than 1 optical or NIR counterpart within a $2''$ radius of the radio position, we choose the counterpart that is nearest the radio position and use its individual SExtractor magnitude, measured within an elliptical aperture corresponding to 2.5 times the Kron radius (Kron 1980). The magnitudes measured in the GOODS dataset in this way are identical to those given by Giavalisco et al. (2004). When multiple GOODS counterparts are available, we choose the nearest source and do not use the ground-based optical data, which is likely to be blended.

3. THE X-RAY FAINT AGN POPULATION

We use the 1.4 GHz and $24 \mu\text{m}$ flux densities of our sample, along with the well-known radio/infrared relation of star-forming galaxies and radio-quiet AGN, to select a sample of radio-excess AGN independently of their X-ray properties. Appleton et al. (2004) define $q = \log(f_{24 \mu\text{m}}/f_{1.4 \text{ GHz}})$. They show for star-forming galaxies that q is tightly constrained out to $z \sim 1$: $q = 0.94 \pm 0.23$ after K-correction. Galaxies with values of q well below this range (strong radio with respect to $24 \mu\text{m}$ emission) are unlikely to be dominated by star formation and instead are radio-emitting AGN (Drake et al. 2003).

which is operated by the Association of Universities for Research in Astronomy, Inc. (AURA) under cooperative agreement with the National Science Foundation

3.1. Sample Selection

Figure 1 illustrates the selection criteria. We set a selection threshold of $q < 0$ to classify a galaxy as probably having an AGN and require a *Chandra* exposure of > 1 Ms to provide high X-ray sensitivity. This selection identifies 27 radio-excess AGN in the CDFN, as listed in Table 1. Of these, 16 (60%) have no X-ray counterpart in the Alexander et al. (2003) catalog.

Because of the lack of spectral information, we have chosen not to K-correct our radio and infrared flux densities and instead illustrate in Figure 1 the redshift evolution of q for galaxies with LINER, Seyfert 2, spiral galaxy, and ultra-luminous infrared galaxy (ULIRG) templates, normalized to the best-fit value of Appleton et al. (2004). Templates were taken from Devriendt et al. (1999). A spectral index of $\alpha = 0.7$ ($S_\nu \propto \nu^{-\alpha}$) was assumed for the radio continuum. For the LINER, Seyfert 2, and spiral templates, the observed q is slightly larger than the intrinsic value out to redshifts of $z \geq 2.7$. Redshifting a ULIRG SED causes the observed q to drop below the intrinsic value as z increases.

Because we have not K-corrected our flux densities, we use the slightly higher non K-corrected dispersion, $\sigma = 0.28$, from Appleton et al. to calculate the significance of our selection threshold at $z = 0$. Our selection threshold of $q < 0$ is 3.4 standard deviations below the average value of q at $z = 0$, and therefore our sample should not be significantly contaminated with normal star-forming galaxies. The significance of our selection at $z > 0$ depends on each object's individual SED, and will increase slightly for LINERS, Seyfert 2's and spirals, but decrease for ULIRGS. We estimate the maximum error on the measured values of q by assuming both a radio and infrared flux density of $80 \mu\text{Jy}$, the approximate limits of our survey. This corresponds to a 5σ $24 \mu\text{m}$ detection and a 10σ radio detection and gives an error of 0.1 on q ; we therefore do not expect our sample to be strongly affected by errors in the flux determination. The crowded nature of several of the fields implies that some of our sources may have blended $24 \mu\text{m}$ emission. This will cause q to increase, however, and will therefore remove sources from our radio excess sample instead of introducing contaminants.

Yun et al. (2001) define radio-excess objects as those with radio emission exceeding the radio/FIR correlation prediction by a factor of ≥ 5 (a behavior hereafter described as a radio excess by a factor of 5). From the measurement of this correlation by Appleton et al. (2004), the corresponding threshold would be $q < 0.24$ at $z = 0$. At $z = 1$, the radio-excess threshold ranges from $q = 0.46$ to $q = 0.53$ for LINER, Seyfert 2, or spiral galaxy templates. For all these cases, our selection criterion of $q < 0$ (which corresponds to a radio excess of 8.7) isolates radio-excess AGN. For a ULIRG template, the radio-excess threshold is -0.30 at $z = 1$; a q of 0 for such a template at $z = 1$ corresponds to a radio excess of 2.5, half the AGN threshold suggested by Yun et al. (2001). As will be discussed in §4, however, a small fraction of the sources in our sample have ULIRG SEDS, and all are likely to be AGN.

Following Drake et al. (2003), radio-loud objects would have $q < -1.6$ at $z = 0$; since few sources fall in this range, the AGN sample consists almost entirely of radio-intermediate sources, as illustrated in the histogram inset in Figure 1.

3.2. Potential Sources of Contamination

At high redshift, the $24 \mu\text{m}$ emission of normal star-forming galaxies is dominated by PAH features, which are absent at

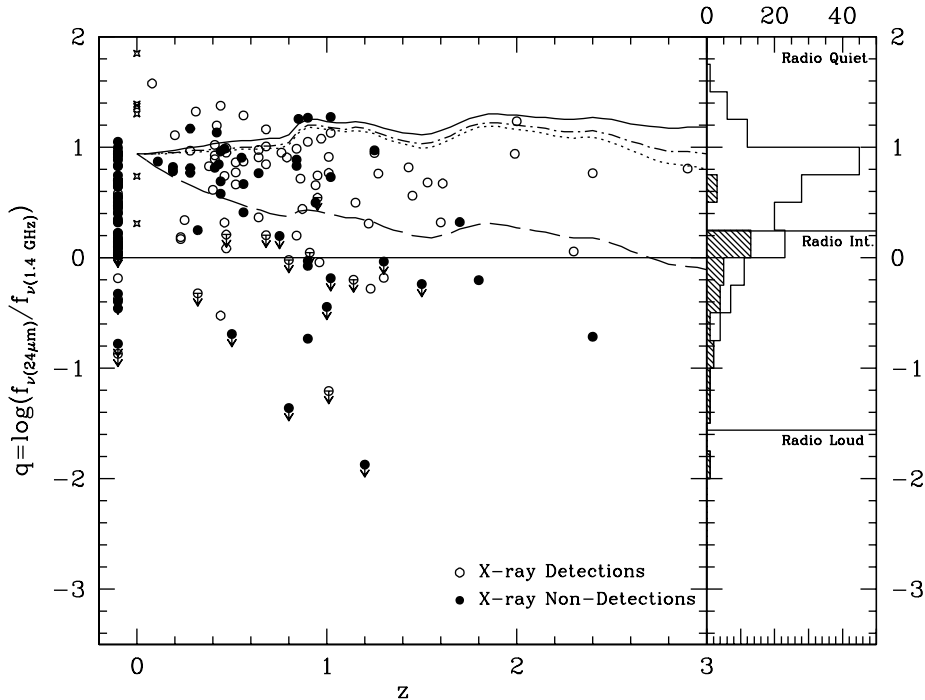


FIG. 1.— Relationship between q and redshift. All sources without known redshifts have been assigned $z = -0.1$. Circles represent all radio sources with X-ray exposures in excess of 1 Ms. Crosses represent the 6 lowest-metallicity galaxies from the Engelbracht et al. (2005) sample. The lines represent the change in the observed q with redshift for SEDs with LINER (solid), Seyfert 2 (dot-dashed), spiral galaxy (dotted), or ULIRG (dashed) templates, normalized to the best-fit local value of q as determined by Appleton et al. (2004). The histogram shows the distributions of q in the radio-quiet, radio-intermediate, and radio-loud regimes, where the shaded histogram represents sources for which we have only upper limits on q , and the clear histogram gives the distribution of q for all sources. We define as our radio-excess AGN sample all galaxies with $q < 0$.

low metallicity (e.g., Houck et al. 2004, Engelbracht et al. 2005). As Figure 1 demonstrates, however, low metallicity star-forming galaxies also tend to have $q > 0$ and therefore they should not contaminate our radio-excess AGN sample.

Nearly all star-forming galaxies in the field fit the radio/infrared correlation. Even within dense galaxy clusters, where environmental effects might boost the radio emission, the relation holds well with only a tiny minority of galaxies having radio excesses as large as a factor of five (Miller & Owen 2001). Bressan et al. (2002) show that a radio excess is expected in post-starburst galaxies due to the slower fading time of the radio emission with respect to the FIR; their models predict a maximum radio enhancement of ~ 5 above the radio/FIR correlation. As mentioned above, our selection criterion selects AGN whose radio enhancements exceed a factor of ~ 9 in LINER, Seyfert 2, and spiral galaxy templates. We therefore expect minimal contamination from post-starburst galaxies.

The strong silicate absorption feature seen in a handful of ULIRGS is another potential source of sample contamination. This feature is centered at $9.7 \mu\text{m}$ and would therefore be redshifted into our $24 \mu\text{m}$ band at redshifts of $z \sim 1.2-1.5$, where it could suppress the observed infrared flux density. Four of the X-ray non-detected radio-excess sample have redshifts in this range.

It is unlikely, however, that a large fraction of AGN are affected in this way. The $12 \mu\text{m}$ flux of AGN provides the best estimate of their bolometric luminosity, allowing for effective infrared selection (Spinoglio & Malkan 1989). The silicate absorption feature is within the IRAS $12 \mu\text{m}$ passband, and

evidently has only a secondary effect on the luminosity estimate. In fact, $\sim 50\%$ of high-luminosity AGN have silicate emission features (Hao et al. 2005). In such cases, the q of true AGN will be shifted towards the star-forming range, resulting in incompleteness in our sample, but not contamination.

3.3. Sample Completeness

Because the 95% completeness limit of the radio sample is equal to the upper limit we can place on the flux densities of non-detected $24 \mu\text{m}$ sources, $80 \mu\text{Jy}$, restricting the radio flux densities to $S_\nu > 80 \mu\text{Jy}$ would provide a 95% complete radio-excess ($q < 0$) sample (subject to the cautions mentioned above). While we do not apply a radio flux-density cut for the sample discussed in this paper, only one AGN in our sample, an X-ray non-detected source, has a radio flux density that falls below this limit. In addition, the counterpart uncertainties and $24 \mu\text{m}$ blending discussed in §2 only led to the removal of one source that could fall into such a complete sample. Therefore, if we were to define a complete sample by requiring that $S_\nu > 80 \mu\text{Jy}$, our sample would essentially remain the same. Also, in §2 we estimated that up to 3 radio-excess AGN would be removed from our sample due to chance coincidences with $24 \mu\text{m}$ sources; this process will reduce the sample size but have no other effect. Thus, we can say that for a sample of 27 radio-excess objects in the CDFN (with X-ray exposures in excess of 1 Ms) that is sufficiently complete to be largely unbiased for this class of AGN, 16 (60%) sources are previously uncatalogued as AGN. The remainder of this paper probes the characteristics of these objects in more detail.

4. REDSHIFTS

Spectroscopic redshifts for 8 AGN, and photometric redshifts for an additional 2, were taken from the literature (Barger et al. 2002, Cowie et al. 2004, Wirth et al. 2004 (TKRS)). The redshifts are tabulated in Table 1 and Figure 1. All but one of the AGN for which Team Keck Redshift Survey (TKRS) spectra are available appear to be early-type galaxies with no obvious signs of nuclear activity in the optical/UV. The remaining source, VLA 123646+621404, is X-ray detected and has weak narrow emission lines.

For most of the remaining AGN in our sample, we estimated redshifts photometrically by fitting the Devriendt et al. (1999) templates to the galaxy optical through MIR spectral energy distributions (SEDs). SED fitting was conducted both by an automated fitting routine and by eye; the two methods give results consistent to within the errors quoted below. The SEDs of all radio-excess AGN in our sample are shown in Figure 2. Pérez-González et al. (2005) provide further details on use of Spitzer and other data to obtain photometric redshifts. The redshifted SED fits are in good agreement with spectroscopic redshifts in all cases where spectroscopic data are available. We are able to find or estimate redshifts for 12 of the 16 X-ray non-detected AGN and for 8 of the 11 X-ray detected AGN. The typical errors in our photometric redshift determinations are $\Delta(z)/(1+z) < 0.1$ (see Pérez-González et al. 2005). The mean redshifts of the X-ray non-detected and X-ray detected AGN samples are $z = 1.2$ and $z = 0.9$, with dispersions of 0.5 and 0.4, respectively.

Source VLA J123642+621331 has a published redshift of $z = 4.42$, based on a single emission line believed to be Ly α (Waddington et al. 1999). The validity of this measurement has been questioned by Barger et al. (2000). In addition, none of the Devriendt et al. templates are able to fit the global SED, so we do not assign a redshift to this source.

The Devriendt et al. templates used to obtain photometric redshifts are comprised of spirals, LINERS, Seyfert 2's, starbursts, and ULIRGS. Of the X-ray non-detected AGN, 9 are best-fit by LINER or Seyfert 2 templates, 2 have ULIRG templates, and 1 appears to be a spiral galaxy. Six of the X-ray detected AGN are best-fit by LINER or Seyfert 2 templates; the remaining 2 are ULIRGS.

With redshifts and fitted SED templates for most of the sample, we can test the robustness of our original $q < 0$ selection. Using the best-fit Devriendt et al. SED templates and the radio spectral slopes from Richards et al. (2000), we estimate the K-corrected radio excesses for the 20 sources with estimated redshifts. All but 1 of the X-ray non-detected AGN (with known redshifts) have radio excesses well above both the Yun et al. "radio-excess" definition of 5 and our $q < 0$ selection, which is equivalent to a radio excess of ~ 9 . The remaining source has a radio excess of 4 and thus should also be dominated by AGN radio emission. Similarly, 6 of the 8 X-ray detected AGN with known redshifts have radio excesses greater than 10; an additional source has a radio excess of 4, and therefore is likely to be AGN-dominated. The remaining source has a radio excess of only 1.3. This source, VLA 123721+621130, is best-fit by a ULIRG template, has an inverted radio spectrum, $\alpha = -0.28$, a very hard X-ray photon index, $\Gamma = 0.28$, and an absorbed X-ray luminosity of $\log L_{0.5-8 \text{ keV}} = 42.7$, all of which indicate the presence of an AGN. We therefore do not remove it from our sample.

5. X-RAY DETECTION AND COADDITION

Although the X-ray non-detected AGN all fall below the Alexander et al. (2003) *Chandra* detection limit, detection to lower significance is possible now that source positions are known *a priori*. We test for X-ray emission by comparing the X-ray counts measured at the positions of our radio sources to the local X-ray background distributions. Four of the X-ray non-detected AGN were excluded from this analysis, as they are separated from known X-ray sources by less than 2 times their 95% encircled energy radii (EER), and are therefore likely to be contaminated. We find signals for 7 of the 12 remaining X-ray "non-detected" AGN at significance levels of 2.5 to 5.2 σ . For the remaining 5 sources, we use a stacking analysis to constrain the average flux. We give details of these measurements below.

5.1. X-ray Detection

To search for X-ray signal from each of the X-ray non-detected AGN, we first extract the total number of X-ray counts within the 60%, 70%, and 80% EER centered on the radio position, using the CDFN 2 Ms image provided by Alexander et al. (2003). The average source exposure time is similarly extracted from the X-ray exposure maps. The EER for the full (0.5-8 keV), hard (2-8 keV), and soft (0.5-2 keV) X-ray bands were calculated using the MKPSF task in CIAO⁴, from which we created an exposure-weighted average PSF for each source, taking into account the sources' positions on the ACIS-I detector during each of the 20 CDFN observations⁵. We assume a photon index of $\Gamma = 1.4$ when calculating the EER, though we have verified that changing this to $\Gamma = 1.0$ negligibly affects the results.

We use a Monte-Carlo simulation similar to that of Brandt et al. (2001) to estimate the local sky background in the 3 X-ray bands and 3 apertures. For each source, we first choose a random position that (1) lies within 1' of the radio source, (2) does not overlap with the source aperture, (3) is a minimum distance of 2 times the source's 95% EER from any cataloged X-ray source, and (4) has an exposure time that differs from the source exposure time by less than 50%. The final condition is set to minimize the effect of large gradients in exposure on our local sky background distributions. To determine the sky background distributions, we measure the sky counts at this random position using the 3 source apertures. We repeat 10,000 times.

Before fitting the sky distributions for each band and EER, we normalize the counts to the source exposure time. We then fit a Poisson distribution to the resulting distributions of normalized background counts, from which we measure the mean sky background. The dispersion of the sky background determines the likelihood of measuring by chance the observed number of counts in an aperture centered on the radio source. We define as "weakly-detected" all sources at $> 2\sigma$ above the background in at least 1 of the 3 *Chandra* energy bands, and in at least 1 of the 3 apertures. Although we require only a $> 2\sigma$ detection, all 7 of the weakly-detected sources are at $> 2.5\sigma$ in at least one of the 3 bands, and 2 are detected to $\geq 5\sigma$. In Table 2, we give the X-ray properties

⁴ *Chandra* Interactive Analysis of Observations (CIAO), <http://cxc.harvard.edu/ciao/>

⁵ At intermediate to large off-axis angles, the CXC PSF libraries crop a small fraction (5-10%) of the X-ray flux, affecting the determination of the EER. We do not attempt to correct for this effect, as the PSFs of the weakly-detected sources are undersampled.

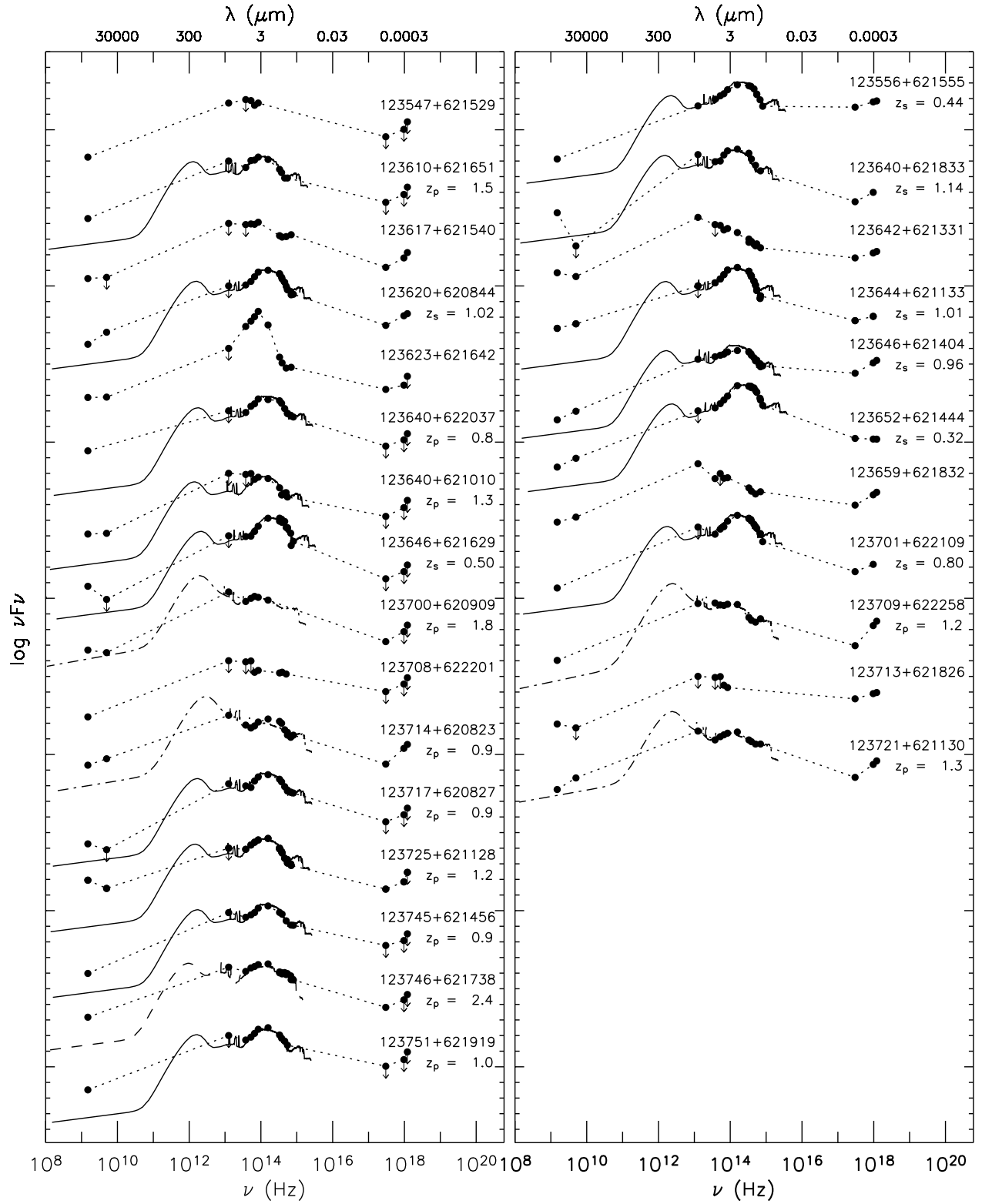


FIG. 2.— Observed-frame SEDs of the radio-excess AGN. Sources with weak or non-detected X-rays are plotted in the left panel, and sources with high-significance X-ray detections are plotted in the right panel. We list VLA source IDs and photometric (z_p) or spectroscopic (z_s) redshifts. Templates were taken from Devriendt et al. (1999). Seyfert 2 and LINER templates are given by solid lines. Dot-dashed lines represent ULIRG templates, and dashed lines represent spiral templates. Large ticks along the y-axis represent an interval of 10 in $\log \nu F_\nu$.

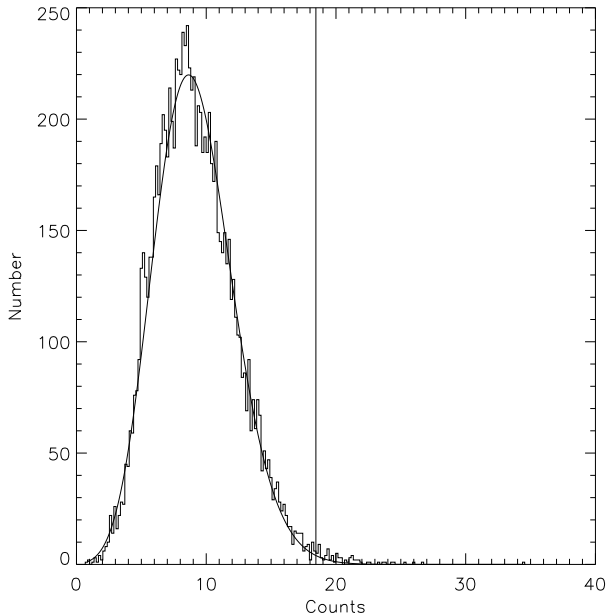


FIG. 3.— X-ray background distribution for source VLA J123617+621540 in the full X-ray band (0.5-8 keV). The counts have been normalized to the source exposure time. The Poisson fit to the background distribution is shown. The vertical line indicates the total number of counts obtained at the source position, and corresponds to a 3σ detection.

of all X-ray weakly-detected AGN. For each source and energy band, we list the results for the aperture (60% EER, 70% EER, or 80% EER) with the highest detection significance. To illustrate our detection method, we show in Figure 3 the X-ray background distribution for VLA J123617+621450, along with the source signal, which corresponds to a 3σ detection.

To calculate the X-ray flux from the aperture-corrected count rate, we first need to know the X-ray photon index, Γ . If a given source is detected to $\geq 2\sigma$ in both the hard and soft X-ray bands, the photon index is estimated from the ratio of the hard to soft count rates, H/S . If a source is not detected to $\geq 2\sigma$ in both the hard and soft bands, we assume that $\Gamma = 1.4$. Although Γ spans a fairly wide range of values for the sources where it can be estimated, the derived fluxes should only be weakly dependent on the value adopted. For consistency, we use the *Chandra* 2 MS Catalog H/S to Γ and X-ray count rate to X-ray flux conversions (Alexander et al. 2003). For comparison with the cataloged fluxes, we do not correct the X-ray fluxes for Galactic absorption. The quoted X-ray flux ratios, however, have been corrected for Galactic absorption of column density $N_{\text{H}} = 1.6 \times 10^{20} \text{ cm}^{-2}$ (Stark et al. 1992).

If a weakly-detected AGN does not have a $\geq 2\sigma$ detection in one or more of the 3 X-ray bands, we quote in Table 2 conservative 2σ upper limits on the count rate and flux. Upper limits were calculated by adding any positive net source counts to 2 times the sky dispersion.

5.2. X-ray Coaddition

For the five sources that are undetected and also a minimum distance of 2 times their 95% EER from the nearest cataloged X-ray source, we determine limits on the X-ray flux by coaddition. Individual source counts are measured as described above, and are then summed to provide the total number of counts from our stacked source. We similarly construct the coadded sky background distribution by adding the individ-

ual sky backgrounds from each of the 10,000 trials.

We list in Table 3 the X-ray properties of the coadded source. Because the detection significance for all 3 X-ray bands is $< 1\sigma$, we list conservative 2σ and 5σ upper limits on the count rates and fluxes, calculated as described above. We also list 2σ and 5σ upper limits on the flux for a "typical" one of these five sources by assuming that an equal amount of flux is coming from each of the sources that contributed to the coaddition.

5.3. X-ray Upper Limits

For all AGN that are not X-ray detected at full band to greater than 2σ , including those that are close to a known X-ray source, we set conservative 5σ upper limits on the X-ray flux by adding any positive source flux to a 5σ limit on the local X-ray background, computed as described above. We use an aperture equal to the 70% EER to measure both the source and background counts. These 5σ X-ray upper limits are used throughout the rest of the paper.

5.4. Column Densities

The column densities to the X-ray detected AGN are given in Table 4. To estimate the column density, we assume that AGN have an intrinsic non-absorbed photon index of $\Gamma = 2$ (e.g., George et al. 2000). We do not include a Compton reflection component in our intrinsic spectral model because of possible dependencies of its strength on luminosity, radio-loudness, and optical Seyfert type (e.g., Lawson & Turner 1997, Reeves & Turner 2000, Zdziarski et al. 1995, Zdziarski et al. 2000). These reflection components have been shown to be important in fitting the peak of the X-ray background (XRB; see Ueda et al. 2003). If a Compton reflection component is added via the 'pexrav' model in XSPEC (Magdziarz & Zdziarski 1995), assuming a solid angle of 2π , a cutoff energy of $E_c = 500 \text{ keV}$, an inclination angle of $\cos i = 0.5$, and solar abundance, the computed column densities decrease by an average of 20%.

Excluding upper limits, the column densities of the X-ray-detected AGN range from $N_{\text{H}} = 1.0 \times 10^{22} \text{ cm}^{-2}$ to $N_{\text{H}} = 3.7 \times 10^{23} \text{ cm}^{-2}$, and are therefore consistent with our definition of obscured AGN. One additional AGN for which we were unable to estimate N_{H} (due to an observed photon index, $\Gamma = 2.1$, that is softer than our assumed photon index) is likely to be relatively unobscured. All of the columns fall below the Compton-thick limit ($N_{\text{H}} > 10^{24} \text{ cm}^{-2}$). If we correct for the Compton-reflection component, 2 of the 11 X-ray detected AGN (20%) are likely to be unobscured.

We list in Table 2 intrinsic column densities for all weakly-detected AGN. For the two X-ray weakly-detected AGN with known flux ratios and redshifts, we calculate column densities of $N_{\text{H}} = 6.8 \times 10^{22} \text{ cm}^{-2}$ and $N_{\text{H}} = 1.6 \times 10^{23} \text{ cm}^{-2}$. We place upper limits on the X-ray column densities of the remaining X-ray weakly-detected AGN. If we have no redshift estimate for a given source, we calculate the column density at redshifts of $z = 0.5$ and $z = 2.5$, the approximate upper and lower redshift bounds of the sources in our sample. All of the column densities fall below the Compton-thick limit.

In Figure 4, we compare the column density distributions of the X-ray detected and weakly-detected AGN. The column densities for AGN with known redshifts and flux ratios are given by cross-hatched histograms. Clear histograms give the column densities for all AGN with known redshifts, including those with upper limits on the flux ratio, and therefore on the column density. There is significant overlap between the

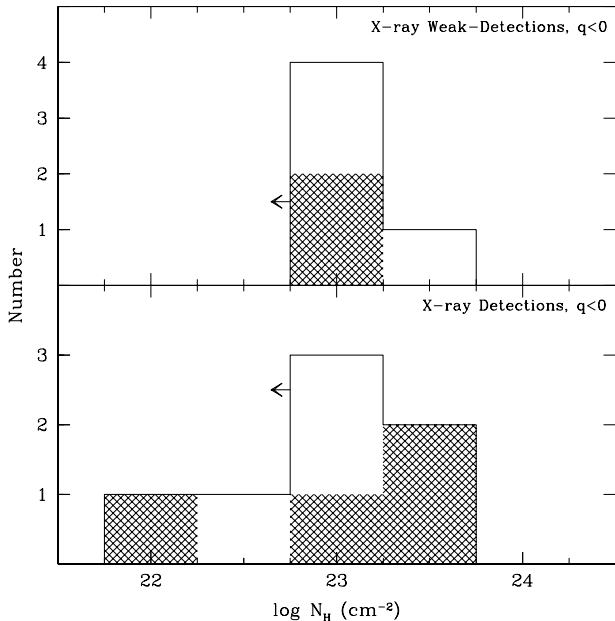


FIG. 4.— Rest-frame column densities measured using the X-ray flux ratios and redshifts of the X-ray weakly-detected and X-ray detected radio-excess AGN samples. The clear histograms represent all sources, including those for which we have only upper limits on N_{H} . The cross-hatched histograms represent only those sources with known N_{H} .

2 samples. The X-ray non-detected AGN are likely to have higher column densities than the weakly-detected sample; if so, there would be a stronger offset between the X-ray detected and X-ray weakly- and non-detected samples.

5.5. Compton-thick AGN

Approximately 50% of Seyfert 2 galaxies in the local Universe are Compton-thick (Risaliti et al. 1999); if we assume a Seyfert 2 to Seyfert 1 ratio of 4:1, the Compton-thick fraction of all local Seyferts is $\sim 40\%$. In the more distant Universe, XRB population synthesis models predict that $\sim 30\%$ of AGN with $N_{\text{H}} < 10^{25} \text{ cm}^{-2}$ have column densities of $N_{\text{H}} = 10^{24} - 10^{25} \text{ cm}^{-2}$ (Comastri et al. 2001). Ueda et al. (2003) similarly find that current measurements of the XRB are consistent with roughly equal numbers of Compton-thick AGN with $N_{\text{H}} = 10^{24} - 10^{25} \text{ cm}^{-2}$ and obscured AGN with $N_{\text{H}} = 10^{23} - 10^{24} \text{ cm}^{-2}$. This ratio is slightly lower than that in local Universe, where there are 1.6 times as many Seyfert 2's with $N_{\text{H}} > 10^{24} \text{ cm}^{-2}$ as Seyferts 2's with $N_{\text{H}} = 10^{23} - 10^{24} \text{ cm}^{-2}$ (Risaliti et al. 1999).

We therefore expect that as many as $\sim 25-40\%$ of the AGN in our radio-selected sample could be Compton-thick. Of the 27 radio-excess AGN, we have placed constraints on the column densities of 13, and have estimated constraints for a further 5 for which no redshift is available. All sources have column densities that fall below the Compton-thick limit. Of the remaining sources in the sample, 5 are X-ray non-detected, and 4 are too close to a known X-ray source to test for low-significance emission. If we assume that (like the sources for which we could test for X-ray emission) $3/4$ of the latter would be X-ray detected, 6 sources in our sample of 27 (22%) could be Compton-thick. This estimate will improve as we increase our sample by extending the current study to additional fields.

6. INTERPRETATION

There is direct evidence, from the determination of X-ray column densities discussed above, that at least several of the X-ray weakly-detected AGN are highly obscured. It appears, however, that many of the X-ray detected AGN also have high column densities. To better understand these two samples, and their relation to one another, we discuss below their radio properties, their X-ray, radio, and infrared luminosity distributions, and the ratios of their X-ray to radio and X-ray to optical emission.

6.1. Radio Extent and Spectral Shape

We give in Table 1 the spatial extent of the radio emission, θ , as determined by Richards et al. (2000). Of the 27 sample members, 1 has no listed extent, 16 are unresolved, and 10 are resolved. There is no significant difference with X-ray flux in the degree of resolution, at least in this small sample. The most highly resolved sources, VLA J123644+621133 and J123725+621128, also have high 1.4 GHz luminosities and very low values of q . It is likely that the large radio spatial extent of these sources is due to powerful radio jets oriented approximately in the plane of the sky. If this is the case, the AGN torus would be oriented edge-on, a condition that would lead to high X-ray obscuration. Nonetheless, the absorption levels of $N_{\text{H}} < 2.0 \times 10^{22} \text{ cm}^{-2}$ and $N_{\text{H}} < 2.0 \times 10^{23} \text{ cm}^{-2}$, respectively, are not exceptionally large. It follows that if the unresolved X-ray weakly- or non-detected AGN are also viewed close to edge-on, as we would expect, they must not have strong extended radio jets. This is not surprising, however, as all but 1 of these AGN (the exception being VLA J123725+621128) have q values that fall short of the radio-loud definition of Yun et al. (2001).

We also list in Table 1 radio spectral slopes for the 17 radio-excess AGN observed at 8.5 GHz by Richards et al. (1998). Following Richards et al. (2000), we define flat spectrum sources as those with $\alpha < 0.5$ and steep spectrum sources as those with $\alpha > 0.5$. Flat spectral slopes are expected for AGN in which synchrotron self-absorption is important. Steep-spectrum emission with a slope of $\alpha = 0.7$ is generally associated with optically thin synchrotron radiation. Of the X-ray weakly- or non-detected AGN, 3 are flat spectrum and 6 are steep spectrum. Five of the X-ray detected AGN are flat spectrum; 3 are steep spectrum. No obvious trend is seen, although the X-ray detected AGN may generally have flatter spectral slopes ($-0.28 < \alpha < 0.94$) than the X-ray non-detected AGN ($0.01 < \alpha < 1.62$). This is consistent with a picture in which our viewing angle to the X-ray detected AGN is aligned closer to the jet axis, resulting in more core-dominated, and therefore flatter, radio emission.

6.2. Radio, 24 μm , and X-ray Luminosities

The 1.4 GHz radio powers, $P_{1.4 \text{ GHz}} = \nu F_{\nu}$, of the radio-excess sample are shown in Figure 5. Because radio emission is not affected by obscuration, the radio power is a measure of the intrinsic power of the sample. The X-ray weakly- or non-detected and X-ray detected AGN span similar ranges of $P_{1.4 \text{ GHz}}$, although the 2 most radio-luminous AGN have been missed in the X-ray. We do not have redshift estimates for 4 of the X-ray weakly- or non-detected AGN and 3 of the X-ray detected AGN; the true power distributions are therefore likely to differ slightly from those presented here.

Within the limitations of the small number of 24 μm detections, the X-ray weakly- or non-detected and X-ray de-

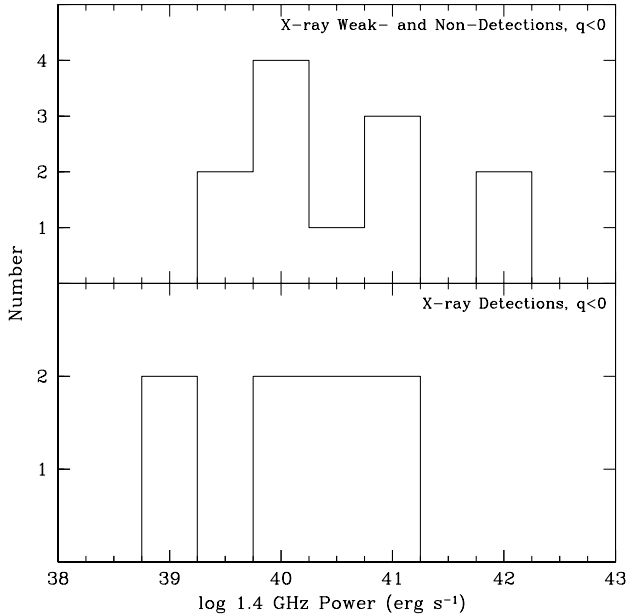


FIG. 5.— 1.4 GHz radio powers of the radio-excess AGN sample.

ected AGN also span similar ranges of 24 μm power. Using the best-fit SEDs from our redshift determinations, we can estimate L_{IR} , the infrared luminosity from 8–1000 μm . We caution that these values are only approximate, as the SEDs in the FIR are not well-constrained by our data. We find that of the X-ray non- and weakly-detected AGN (with redshift estimates), 1 is a ULIRG ($L_{\text{IR}} > 10^{12} L_{\odot}$), 2 are LIRGS ($10^{11} L_{\odot} < L_{\text{IR}} < 10^{12} L_{\odot}$), 8 have luminosities of $10^{10} L_{\odot} < L_{\text{IR}} < 10^{11} L_{\odot}$, and 1 has a luminosity that falls below $10^{10} L_{\odot}$. Two of the X-ray detected AGN are ULIRGS, 1 is a LIRG, 3 have luminosities of $10^{10} L_{\odot} < L_{\text{IR}} < 10^{11} L_{\odot}$, and 2 have a luminosity that falls below $10^{11} L_{\odot}$.

The 0.5–8 keV X-ray luminosities of our radio-excess sample are shown in Figure 6. For all sources with column density estimates, we calculate absorption-corrected X-ray luminosities, assuming an intrinsic photon index of $\Gamma = 2$. The results are listed in Tables 2 and 4. They are subject to relatively large errors, given the uncertainties in the measurements of Γ at low signal to noise as well as possible intrinsic variations in the photon index. They are nonetheless useful as rough estimates. Because there is no X-ray K-correction for a spectrum with $\Gamma = 2$, rest-frame 0.5–8 keV luminosities are equivalent to observed-frame, absorption-corrected 0.5–8 keV luminosities. We overplot on Figure 6, as solid lines, the rest-frame 0.5–8 keV X-ray luminosities of all sources with known redshifts and column density estimates. We see that of the AGN for which we can estimate intrinsic luminosities, those with the highest luminosities were detected in the X-ray. Low-luminosity AGN (LLAGN), however, were also detected in the X-ray; one such source, VLA J123652+621444, has an X-ray luminosity of $L_{0.5-8 \text{ keV}} = 1.6 \times 10^{41} \text{ erg s}^{-1}$ and an optical through MIR SED that is well fit by a LINER template.

6.3. Observed X-ray vs. Radio Emission

The ratio of X-ray to radio emission provides another probe of the nature of sources in our sample. We define $q' = \log(f_{1.4 \text{ GHz}}/f_{4 \text{ keV}})$ and compute the X-ray flux densities at an en-

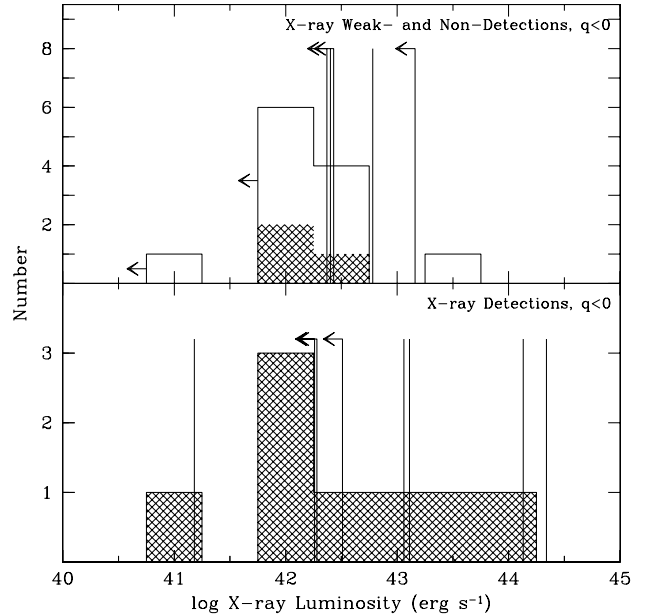


FIG. 6.— Observed X-ray luminosity distributions of the radio-excess AGN sample. The clear histograms represent all sources, including those for which we have only upper limits on $L_{0.5-8 \text{ keV}}$. The cross-hatched histograms represent only those sources with known $L_{0.5-8 \text{ keV}}$. For those AGN for which we can estimate N_{H} , we overplot as solid lines the intrinsic 0.5–8 keV absorption-corrected X-ray luminosities.

ergy of 4 keV (assuming a photon index of $\Gamma = 1.7$, equivalent to a spectral index of $\alpha = 0.7$, for a bandpass correction). Since a typical radio spectrum has a slope of $\alpha = 0.7$ ($S_{\nu} \propto \nu^{-\alpha}$), we do not apply any K-corrections to the ratio of radio to X-ray flux density. Thus, the values we use are as close as possible to the observed radio vs. the observed X-ray flux densities. Figure 7 shows the distribution of q' for our X-ray detected and non-detected AGN samples, along with all X-ray detections that meet our exposure cut.

To compare with a control sample, we have also plotted q' for the X-ray detected (with ASCA) radio sample of Sambruna et al. (1999). This study is of representative sources, not of a complete well-defined sample, and contains 28 objects with sufficient data to be plotted (of 38; the omitted sources are 3C 99, 3C 275, 3C 295, 3C 330, 3C 368, 3C 411, 4C +41.17, 4C +55.16, 4C +74.26, PKS 0625-53, and NGC 6251). All but four of the plotted sources are at $z \sim 0.3$ or less. All the objects for which IRAS 25 μm data are available have $q < 0$ and are therefore AGN by the same criterion used in this paper. Of the 28 sources, 16 are radio-intermediate ($q > -1.6$) and four more are only slightly more radio luminous ($-1.6 > q > -2$). They therefore are reasonable to compare with our predominantly radio-intermediate sources.

We have also included sources from Gambill et al. (2003). This study uses *Chandra* data for bright quasars over a large range of redshift. The sample is mostly useful to augment the statistics for radio quasars, which are not well represented in the Sambruna et al. work.

Figure 7 shows that the overall behavior of q' is as one might expect from selection biases: a sample of AGN selected in the X-ray tends to be relatively brighter in X-rays compared with the radio than does a sample of AGN selected in the radio (i.e. the control sample). Because our use of q' normalizes both samples to radio flux density, this behavior re-

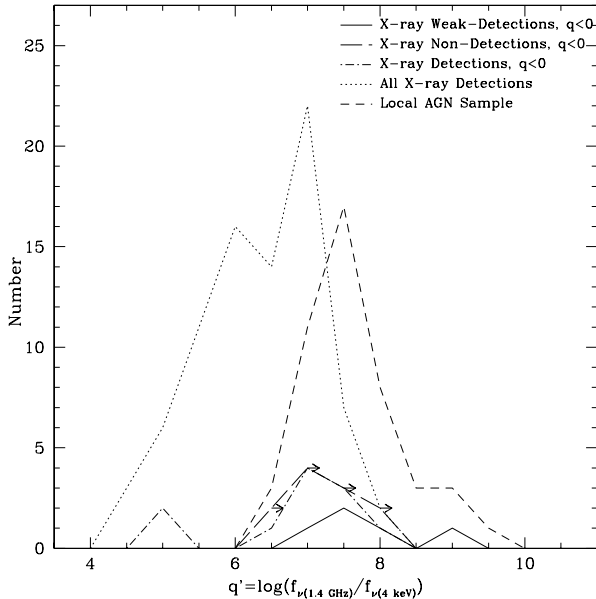


FIG. 7.— Histogram of q' . X-ray detections, weak detections, and non-detections are samples as defined in this paper. The "local" sample is from Sambruna et al. (1999), augmented by Gambill et al. (2003). The sample labeled "all X-ray detections" represents the X-ray sources in the CDFN that have radio counterparts in the catalog of Richards (2000). For viewing clarity, we do not plot the full histograms, but instead connect their values at the bin centers.

flects an intrinsic difference in radio-to-X-ray spectral energy distributions, and is not simply an effect of low-luminosity radio sources without X-ray counterparts. *If the local radio-detected sample has analogs at higher redshift, as expected, they would fall below the current Chandra detection limit, yielding incomplete samples in the X-ray.*

The q' distribution of the 5 X-ray weakly-detected sources is clearly more consistent with that of the control sample than the full *Chandra*-detected sample. The q' distributions also suggest that some fraction of our X-ray non-detected AGN are more similar in nature to these local AGN than they are to the full *Chandra*-detected sample. In contrast, the radio-excess X-ray detected AGN sample is more consistent with the overall *Chandra*-detected sample than with the local AGN sample. A two-sided Kolmogorov-Smirnov (KS) test gives a probability of 4% that the full *Chandra*-detected and radio-excess X-ray detected AGN are drawn from the same sample. The corresponding probability for the *Chandra*-detected and radio-excess X-ray weakly-detected AGN sample is 0.2%.

The large values of q' for the control sample and the X-ray weakly- or non-detected sample could be due to intrinsically lower X-ray to radio luminosity, to heavy obscuration, or to some combination of the two. We test the obscuration hypothesis by comparing R , the ratio of compact to total radio emission, to q' for the control sample. The compactness, $\log R$, is often used as an indication of the orientation of the radio source relative to the observer. If the source is viewed down the jet axis, $\log R = 0$, and the flux is dominated by beamed emission. As the viewing angle moves away from the jet axis, $\log R$ becomes more negative.

Figure 8 compares $\log R$ to q' for all of the control sample except 3C28. We have excluded this object because the X-ray emission from its position appears to be strongly dominated by emission by its galaxy cluster, not the AGN (Hardcastle &

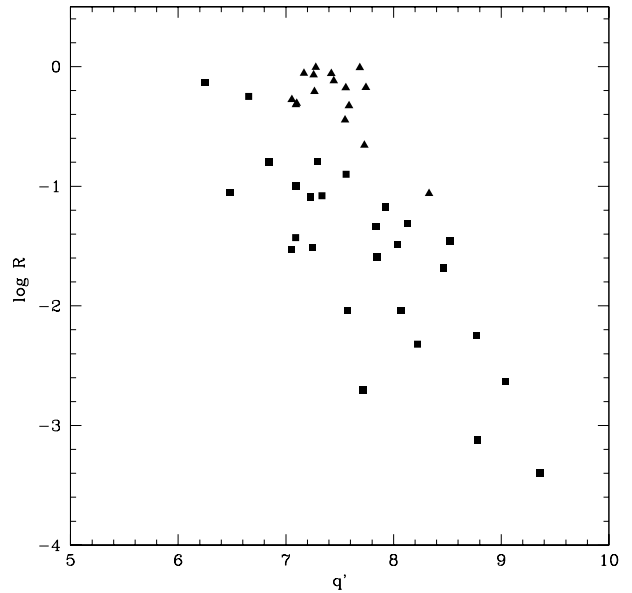


FIG. 8.— Relationship between $\log R$, the ratio of compact to total radio emission, and q' for the local AGN samples of Sambruna et al. (1999; squares) and Gambill et al. (2003; triangles).

Worrall 1999). There is a strong correlation in the sense that the more negative $\log R$, the larger q' . That is, the more the radio jets are aligned away from the observer, the weaker the X-rays are relative to the radio. This behavior is consistent with a standard unification model where the circumnuclear torus plays an increasing role in absorbing the X-rays as the viewing angle of the central accretion disk approaches edge-on. The parameter q' therefore appears to be correlated with viewing angle, and consequently with obscuration, in local samples. We note that the 2 highly radio-resolved sources discussed in §6.1 also have the highest values of q' , a result that is consistent with the above interpretation. The relatively high limits on q' for the X-ray non-detected AGN therefore suggest that the beamed radio emission of these AGN is aligned away from us, increasing their likelihood of being heavily obscured.

6.4. Intrinsic X-ray vs. Radio Emission

We plot in Figure 9 the intrinsic X-ray to radio emission ratios, q'_{corr} , for the X-ray weakly-detected and X-ray detected samples. We calculate q'_{corr} by correcting the observed 0.5–8 keV X-ray flux for the estimated column densities. We assume a photon index of $\Gamma = 2$ when applying this correction. Because the radio spectral slopes are known for the majority of the sources for which we have column density estimates, we apply a radio K-correction, such that $q'_{\text{corr}} = \log(f_{1.4 \text{ GHz}}/f_{4 \text{ keV, corr}}) + (\alpha_{\text{radio}} - 1)\log(1+z)$. We list the values of q'_{corr} in Tables 2 and 4. For sources without known radio spectral indices, we assume $\alpha = 0.7$.

The X-ray detected sample has, on average, a lower q'_{corr} than the X-ray non-detected sample, although there is a significant amount of overlap between the 2 samples and many of the sources have only lower limits on q'_{corr} . This suggests, however, that some fraction of the X-ray detected sample may have intrinsically higher X-ray luminosities (with respect to their radio luminosities) than do sources that were not detected in the X-ray. Such a conclusion is in agreement with the absorption-corrected X-ray luminosities, which are gener-

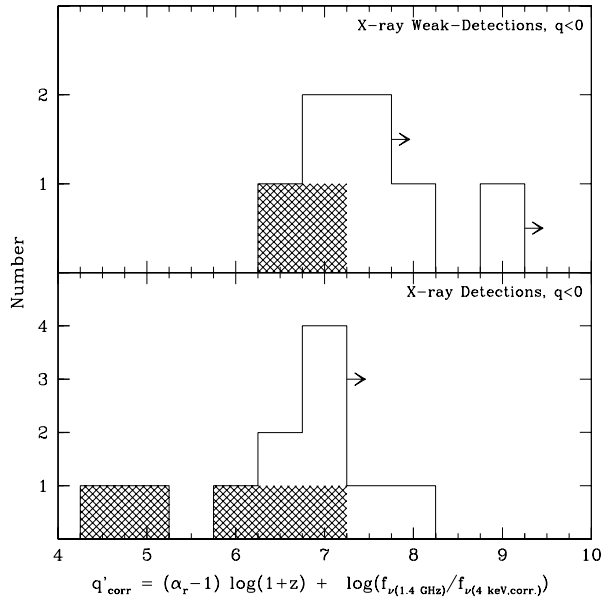


FIG. 9.— Histogram of the absorption- and K-corrected q' . The clear histograms represent all sources, including those for which we have only lower limits on q'_{corr} . The cross-hatched histograms represent only those sources with known q'_{corr} .

ally higher for the X-ray-detected AGN. A sample of intrinsically X-ray weak AGN with hard X-ray spectra was studied by Risaliti et al. (2003), who suggest that such objects could contribute significantly to the hard component of the X-ray background. Unfortunately, because we do not have column density estimates for the X-ray non-detected sources, it is unclear whether this trend will hold for the entire sample.

It is also possible that a selection effect is responsible for the apparently lower intrinsic X-ray luminosities of the X-ray weakly-detected sample. Because the X-ray detected and X-ray weakly-detected samples span similar ranges of column densities, it is likely that the AGN that were previously X-ray detected are those that are intrinsically the most luminous.

6.5. X-ray vs. Optical Emission

The optical to X-ray emission ratio is a powerful diagnostic for distinguishing AGN from star-forming galaxies (e.g. Maccacaro et al. 1988). AGN typically lie within $\log f_X/f_R = \pm 1$; at the highest fluxes probed by the CDFN, the mean AGN flux ratio is consistent with $\log f_X/f_R = 0$, whereas at lower fluxes, the mean ratio rises slightly due to increased optical obscuration (Barger et al. 2003). Starbursts and lower-luminosity AGN populate the transition region ($-2 < \log f_X/f_R < -1$), whereas normal star-forming galaxies, starbursts, and LLAGN typically have X-ray to optical flux ratios of $\log f_X/f_R < -2$ (see Barger et al. 2003, Hornschemeier et al. 2003).

Figure 10 shows the observed R-band magnitudes and hard (2–8 keV) X-ray fluxes of our radio-excess AGN sample. We place a lower limit of $R=25.0$ mag on sources with no R-band counterpart. For sources with multiple GOODS counterparts, but only a single ground-based R-band counterpart, we treat the R-band magnitude as a lower limit.

Of the 11 hard X-ray-detected radio-excess AGN, all but 1 lie within the AGN or transition regions, as expected. The source that lies in the quiescent galaxy region is the LLAGN,

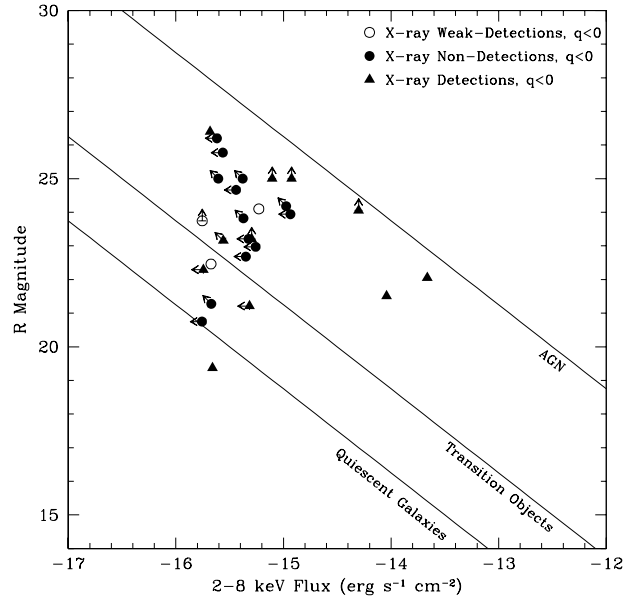


FIG. 10.— Relationship between the observed R magnitude and 2–8 keV (hard band) X-ray flux. X-ray detected sources are given by triangles, and X-ray weakly- and non-detected sources by circles. The lines represent the regions populated by AGN ($f_X/f_R < |1|$), AGN and starbursts ($-2 < \log f_X/f_R < -1$), and quiescent galaxies, starbursts, and LLAGN ($\log f_X/f_R < -2$) (see Barger et al. 2003, Hornschemeier et al. 2003).

VLA J123652+621444, discussed in §6.2. The current X-ray and optical limits also place the X-ray weakly- and non-detected AGN primarily in the AGN region, with 3 extending into the transition region. Higher sensitivity X-ray observations are needed to determine the true locations of the sample. Given the current limits, however, all 16 sources are consistent with the predictions for normal AGN.

7. CONCLUSIONS

We define a sample of 27 radio-excess AGN in the CDFN by selecting galaxies that do not obey the radio/infrared relation for star-forming galaxies and radio-quiet AGN. Sixteen (60%) of these AGN are previously undetected at X-ray exposures of > 1 Ms, although we have subsequently detected X-ray signals from 7 more at significance levels of 2.5 to 5.2 σ . In this paper, we examine the characteristics of these 16 X-ray weak AGN, and their relationship to the 11 AGN previously detected in the X-ray. We find:

- The values and limits we place on N_H for the X-ray weak AGN are all consistent with their being obscured, but not Compton-thick (i.e., $10^{22} \text{ cm}^{-2} < N_H < 10^{24} \text{ cm}^{-2}$). Of the 9 AGN that are either X-ray non-detected or are too close to a known X-ray source to search for weak X-ray emission, we estimate that 6 could be Compton thick. This corresponds to 22% of our sample and is consistent with predictions from the X-ray background.
- The column densities to the X-ray-detected members of our sample are similar to those of the X-ray weak AGN, although they extend to lower absorbing column. All but 1 (or 2 if a Compton reflection component is considered) fall in the range of obscured but not Compton-thick AGN. This corresponds to 80% of the sample, and is consistent with predictions that X-ray obscured AGN

outnumber non-obscured AGN by a factor of 4:1. If we assume that all of the X-ray non-detected AGN are obscured, however, the overall fraction of obscured AGN rises to 93%.

- The ratio of radio to X-ray emission indicates that orientation of the circumnuclear torus, and therefore obscuration, is at least partly responsible for attenuating the X-ray fluxes, as we would expect. To support this scenario, we show that a local sample of radio AGN has a ratio of radio to X-ray emission that shows a dependence on viewing angle consistent with the effects of X-ray absorption by a circumnuclear torus.
- Indicators such as the ratio of optical to X-ray emission, the intrinsic absorption-corrected X-ray luminosities, and the radio luminosities all support the argument that the weak X-ray sources are similar in intrinsic properties to the AGN selected in a similar way but with stronger X-ray fluxes. This similarity would be strengthened by the usual tendency that any sample se-

lected in a given spectral band (e.g., X-ray or radio) will tend to include preferentially the sources of a given population that are relatively brighter in that band.

In summary, $\sim 60\%$ of radio-excess AGN have been missed in the CDFN survey at X-ray exposures > 1 Ms. At least $1/2$ of the radio-excess AGN have high, but not extreme column densities ($10^{22} \text{ cm}^{-2} < N_H < 10^{24} \text{ cm}^{-2}$), and X-ray, radio, and infrared luminosities similar to those of normal radio-excess X-ray detected AGN. Six (22%) of the sample may be Compton thick ($N_H > 10^{24} \text{ cm}^{-2}$). These results are consistent with proposals that obscured AGN outnumber unobscured ones by $\sim 4:1$, although the proportion of potentially Compton-thick objects is at the low end of the predictions.

This work was supported by an NSF Graduate Research Fellowship and by NASA through contract 960785 issued by JPL/California Institute of Technology. We thank Franz Bauer for an exceptionally detailed and helpful referee report.

REFERENCES

- Alexander, D. M. et al. 2003, *AJ*, 126, 539
 Appleton, P. N. et al. 2004, *ApJS*, 154, 147
 Barger, A. J., Cowie, L. L., & Richards, E. A. 2000, *AJ*, 119, 2092
 Barger, A. J., Cowie, L. L., Brandt, W. N., Capak, P., Garmire, G. P., Hornschemeier, A. E., Steffen, A. T., & Wehner, E. H. 2002, *AJ*, 124, 1839
 Barger, A. J. et al. 2003, *AJ*, 126, 632
 Bertin, E. & Arnouts, S. 1996, *A&AS*, 117, 393
 Brandt, W. N., Hornschemeier, A. E., Schneider, D. P., Alexander, D. M., Bauer, F. E., Garmire, G. P., & Vignali, C. 2001, *ApJ*, 558, L5
 Bressan, A., Silva, L., & Granato, G. L. 2002, *A&A*, 392, 377
 Capak, P. et al. 2004, *AJ*, 127, 180
 Comastri, A., Fiore, F., Vignali, C., Matt, G., Perola, G. C., La Franca, F. 2001, *MNRAS*, 327, 781
 Cowie, L. L., Barger, A. J., Hu, E. M., Capak, P., & Songaila, A. 2004, *AJ*, 127, 3137
 Devriendt, J. E. G., Guiderdoni, B., & Sadat, R. 1999, *A&A*, 350, 381
 Drake, C. L., McGregor, P. J., Dopita, M. A., & van Breugel, W. J. M. 2003, *AJ*, 126, 2237
 Engelbracht, C. W. 2004, *ApJL*, submitted
 Fazio, G. G. et al. 2004, *ApJS*, 154, 10
 Gambill, J. K., Sambruna, R. M., Chartas, G., Cheung, C. C., Maraschi, L., Tavecchio, F., Urry, C. M., & Pesce, J. E. 2003, *A&A*, 401, 505
 George, I. M., Turner, T. J., Yaqoob, T., Netzer, H., Laor, A., Mushotzky, R. F., Nandra, K., & Takahashi, T. 2000, *ApJ*, 531, 52
 Giavalisco, M. et al. 2004, *ApJ*, 600, 93
 Gilli, R. 2004, *Adv. Space Res.*, 34, 2470
 Gordon, K. D. et al. 2004, *ApJS*, 154, 215
 Hao, L. et al. 2005, *ApJL*, in press
 Hardcastle, M. J. & Worrall, D. M. 1999, *MNRAS*, 309, 969
 Helou, G., Soifer, B. T., & Rowan-Robinson, M. 1985, *ApJL*, 298, L7
 Hornschemeier, A. E. et al. 2003, *AJ*, 126, 575
 Houck, J. R. et al. 2004, *ApJS*, 154, 211
 Huang, J.-S. et al. 2004, *ApJS*, 154, 44
 Kron, R. G. 1980, *ApJS*, 43, 305
 Lawson, A. J. & Turner, M. J. L. 1997, *MNRAS*, 288, 920
 Maccacaro, T., Gioia, I. M., Wolter, A., Zamorani, G., & Stocke, J. T. 1988, *ApJ*, 326, 680
 Magdziarz, P. & Zdziarski, A. A. 1995, *MNRAS*, 273, 837
 Maiolino, R. & Rieke, G. H., 1995, *ApJ*, 454, 95
 Maiolino, R., Salvati, M., Bassani, L., Dadina, M., della Ceca, R., Matt, G., Risaliti, G., & Zamorani, G. 1998, *A&A*, 338, 781
 Miller, N. A. & Owen, F. N. 2001, *AJ*, 121, 1903
 Papovich, C. et al. 2004, *ApJS*, 154, 70
 Pérez-González, P. G. et al. 2005, *ApJ*, submitted
 Reeves, J. N. & Turner, M. J. L. 2000, *MNRAS*, 316, 234
 Richards, E. A., Kellermann, K. I., Fomalont, E. B., Windhorst, R. A., & Partridge, R. B. 1998, *AJ*, 116, 1039
 Richards, E. A. 2000 *ApJ*, 533, 611
 Risaliti, G., Maiolino, R., & Salvati, M. 1999, *ApJ*, 522, 157
 Risaliti, G., Elvis, M., Gilli, R., & Salvati, M., 2003, *ApJ*, 587, L9
 Sambruna, R. M., Eracleous, M., & Mushotzky, R. F., 1999, *ApJ*, 526, 60
 Spinoglio, L. & Malkan, M. A. 1989, *ApJ*, 342, 83
 Stark, A. A., Gammie, C. F., Wilson, R. W., Bally, J., Linke, R. A., Heiles, C., & Hurwitz, M. 1992, *ApJS*, 79, 77
 Treister, E. et al. 2004, *ApJ*, 616, 123
 Ueda, Y., Akiyama, M., Ohta, K., & Miyaji, T. 2003, *ApJ*, 598, 886
 Waddington, I., Windhorst, R. A., Cohen, S. H., Partridge, R. B., Spinrad, H., & Stern, D., 1999, *ApJ*, 526, L77
 Wirth, G. D. et al. 2004, *AJ*, 127, 3121
 Yun, M. S., Reddy, N. A., & Condon, J. J. 2001, *ApJ*, 554, 803
 Zdziarski, A. A., Poutanen, J. & Johnson, W. N. 2000, *ApJ*, 542, 703
 Zdziarski, A. A., Johnson, W. N., Done, C., Smith, D. & McNaron-Brown, K. 1995, *ApJ*, 438, L63

TABLE 1
RADIO, 24 μ M, AND X-RAY PROPERTIES

α_{2000}	δ_{2000}	z	1.4 GHz flux (μ Jy)	log 1.4 GHz Power (erg s^{-1})	24 μ m flux (μ Jy)	log 24 μ m Power (erg s^{-1})	X-ray ^a flux ($\text{erg cm}^2 \text{ s}^{-1}$)	log X-ray Luminosity (erg s^{-1})	q	q'	α	θ ($''$)	z Ref.
X-ray Weakly-Detected and Non-Detected AGN													
12 35 47.96	62 15 29.2	...	118	...	40.8	...	$<2.28 \times 10^{-16}$...	-0.46	>7.1	...	<2.1	...
12 36 10.57	62 16 51.6	1.5	139	40.4	<80	<44.1	$<1.57 \times 10^{-16}$	<42.3	<-0.24	>7.3	...	2.7	7
12 36 17.57	62 15 40.7	...	200	...	<80	...	1.33×10^{-16}	...	<-0.40	7.5	>0.55	<2.0	...
12 36 20.28	62 08 44.1	1.02	123	40.0	<80	<43.7	2.56×10^{-16}	42.1	<-0.19	7.0	0.01 ± 0.07	<2.1	1,2
12 36 23.54	62 16 42.7	...	481	...	<80	...	9.64×10^{-17}	...	<-0.78	8.0	0.63 ± 0.07	<1.9	...
12 36 40.15	62 20 37.4	0.8	1840	40.9	<80	<43.5	$<3.02 \times 10^{-16}$	<41.9	<-1.36	>8.1	...	<1.9	7
12 36 40.74	62 10 10.6	1.3	86.8	40.1	<80	<44.0	$<1.38 \times 10^{-16}$	<42.1	<-0.04	>7.1	0.44 ± 0.15	3.7	7
12 36 46.34	62 16 29.6	0.50	393	39.7	<80	<43.0	$<1.10 \times 10^{-16}$	<41.0	<-0.69	>7.9	>1.62	2.7	1,2
12 37 00.26	62 09 9.8	1.8	324	41.0	203	44.7	$<1.57 \times 10^{-16}$	<42.5	-0.20	>7.7	0.89 ± 0.12	<2.0	7
12 37 08.78	62 22 01.9	...	170	...	<80	...	$<6.97 \times 10^{-16}$...	<-0.33	>6.7	...	<2.1	...
12 37 14.96	62 08 23.5	0.9	1380	40.9	255	44.1	5.97×10^{-16}	42.4	-0.73	7.7	0.15 ± 0.08	<1.9	7
12 37 17.53	62 08 27.7	0.9	126	39.9	106	43.7	$<3.00 \times 10^{-16}$	<42.1	-0.08	>7.0	>0.77	2.1	7
12 37 25.73	62 11 28.5	1.2	5960	41.8	<80	<43.9	1.50×10^{-16}	42.1	<-1.87	9.0	1.35 ± 0.06	5.5	7
12 37 45.73	62 14 56.3	0.9	63.6	39.6	59.4	43.5	$<2.64 \times 10^{-16}$	<42.0	-0.03	>6.7	7
12 37 46.60	62 17 38.4	2.4	998	41.8	192	45.0	$<4.22 \times 10^{-16}$	<43.3	-0.72	>7.7	...	<1.9	7
12 37 51.21	62 19 19.1	1.0	223	40.2	<80	<43.7	$<6.25 \times 10^{-16}$	<42.5	<-0.45	>6.9	...	<2.0	7
X-ray Detected AGN													
12 35 56.05	62 15 55.6	0.44	89.7	38.9	26.8	42.3	1.31×10^{-14}	42.9	-0.52	5.2	...	2.5	3
12 36 40.6	62 18 33	1.14	324	40.5	<205	<44.2	2.13×10^{-16}	42.2	<-0.20	7.5	>0.8	<2.0	1
12 36 42.09	62 13 31.4	...	467	...	197	...	2.76×10^{-16}	...	-0.37	7.6	0.94 ± 0.06	2.2	4,5
12 36 44.39	62 11 33.1	1.01	1290	41.0	<80	<43.7	2.44×10^{-16}	42.1	<-1.21	8.1	0.3 ± 0.05	12	1,2
12 36 46.34	62 14 4.7	0.96	179	40.1	162	44.0	2.46×10^{-14}	44.0	-0.04	5.2	-0.04 ± 0.06	<2.0	1,2
12 36 52.92	62 14 44.0	0.32	168	38.9	<80	<42.5	4.63×10^{-16}	41.2	<-0.32	6.9	-0.12 ± 0.07	2.5	1,2
12 36 59.15	62 18 32.8	...	506	...	329	...	8.76×10^{-16}	...	-0.19	7.1	0.26 ± 0.07	<2.0	...
12 37 1.10	62 21 9.6	0.8	304	<40.1	<289	<44.0	3.22×10^{-16}	42.0	<-0.02	7.3	...	<2.0	1,2
12 37 9.94	62 22 58.9	1.23	708	40.9	370	44.6	5.21×10^{-15}	43.6	-0.28	6.5	...	<1.9	6
12 37 13.87	62 18 26.5	...	595	...	<80	...	1.69×10^{-15}	...	<-0.87	6.9	>0.92	<1.9	...
12 37 21.25	62 11 30.0	1.3	382	40.7	250	44.5	5.09×10^{-16}	42.7	-0.18	7.2	-0.28 ± 0.06	0.9	7

REFERENCES. — (1) Cowie et al. 2004 (Hawaii); (2) Wirth et al. 2004 (TKRS); (3) Barger et al. 2002; (4) Waddington et al. 1999; (5) Barger et al. 2000; (6) Barger et al. 2003 (photometric); (7) our photometric estimate

^a 5σ upper limits are given for all AGN that were not weakly-detected in the X-ray (see §5.3)

TABLE 2
X-RAY PROPERTIES OF X-RAY WEAKLY-DETECTED AGN

Source	z	Nearest X-ray Source ^a	X-ray Band	EER (%)	Detection σ	Aperture Corrected Count Rate (s ⁻¹)	H/S	Γ	Flux (erg s ⁻¹ cm ⁻²)	Hard/Soft Flux Ratio	N _H (cm ⁻²)	Abs. Corrected log L _{0.5-8 keV} (erg s ⁻¹)	q' _{corr}
VLA J123617+621540	...	20.4(4.3)	Full	70	3.1	7.06×10^{-06}	1.5	0.47	1.33×10^{-16}	8.6	$(5.0 \times 10^{22} - 5.6 \times 10^{23})$	(41.4-43.2)	7.2-7.0
			Hard	80	2.5	6.14×10^{-06}			1.76×10^{-16}			(41.3-43.1)	
			Soft	60	3.9	4.15×10^{-06}			1.99×10^{-17}			(41.3-43.1)	
VLA J123620+620844	1.02	29.5(5.6)	Full	60	3.6	1.60×10^{-05}	1.0	0.80	2.56×10^{-16}	5.4	6.8×10^{22}	42.4	6.5
			Hard	60	2.1	8.02×10^{-06}			2.12×10^{-16}			42.1	
			Soft	60	3.5	7.79×10^{-06}			3.78×10^{-17}			42.1	
VLA J123623+621642	...	14.3(3.1)	Full	60	3.6	8.27×10^{-06}	<0.7	>1.09	9.64×10^{-17}	<3.3	$(<1.8 \times 10^{22} - <1.8 \times 10^{23})$	(<41.2-<42.9)	>7.9->7.7
			Hard	70	0.9	$<4.56 \times 10^{-06}$			$<1.05 \times 10^{-16}$			(<41.0-<42.8)	
			Soft	60	5.2	6.12×10^{-06}			3.07×10^{-17}			(<41.0-<42.8)	
VLA J123700+620909	1.8	31.2(5.9)	Full	60	0.7	$<5.36 \times 10^{-06}$	<1.3	>0.60	$<6.25 \times 10^{-17}$	<5.7	$<1.9 \times 10^{23}$	<42.4	>7.8
			Hard	80	-0.7	$<5.57 \times 10^{-06}$			$<1.28 \times 10^{-16}$			<42.5	
			Soft	70	2.5	4.33×10^{-06}			2.17×10^{-17}			<42.5	
VLA J123714+620823	0.9	27.2(3.7)	Full	60	5.0	2.46×10^{-05}	2.7	-0.06	5.97×10^{-16}	17.7	1.6×10^{23}	42.8	7.1
			Hard	60	4.2	1.82×10^{-05}			5.91×10^{-16}			42.5	
			Soft	60	2.8	6.83×10^{-06}			3.26×10^{-17}			42.5	
VLA J123725+621128	1.2	31.1(5.4)	Full	80	2.9	1.29×10^{-05}	<1.4	>0.53	1.50×10^{-16}	<6.1	$<1.0 \times 10^{23}$	<42.4	>8.8
			Hard	70	1.5	$<8.52 \times 10^{-06}$			$<1.96 \times 10^{-16}$			<42.2	
			Soft	80	2.8	6.15×10^{-06}			3.08×10^{-17}			<42.2	
VLA J123746+621738	2.4	44.1(5.2)	Full	60	1.8	$<1.69 \times 10^{-05}$	<0.7	>1.12	$<1.97 \times 10^{-16}$	<3.2	$<1.6 \times 10^{23}$	<43.2	>7.7
			Hard	80	0.0	$<1.18 \times 10^{-05}$			$<2.72 \times 10^{-16}$			<43.1	
			Soft	70	4.1	1.65×10^{-05}			8.27×10^{-17}			<43.1	

^aNearest X-ray source in arcseconds and ratio of this distance to the hard-band 95% encircled energy aperture radius

TABLE 3
LIMITS ON THE X-RAY FLUX OF 5 X-RAY NON-DETECTED AGN

Band	2σ Flux Limit ($\text{erg s}^{-1} \text{cm}^{-2}$)	5σ Flux Limit ($\text{erg s}^{-1} \text{cm}^{-2}$)	2σ Individ. Flux Limit ($\text{erg s}^{-1} \text{cm}^{-2}$)	5σ Individ. Flux Limit ($\text{erg s}^{-1} \text{cm}^{-2}$)
Full	$<4.11 \times 10^{-16}$	$<8.42 \times 10^{-16}$	$<8.23 \times 10^{-17}$	$<1.68 \times 10^{-16}$
Hard	$<6.50 \times 10^{-16}$	$<1.41 \times 10^{-15}$	$<1.30 \times 10^{-16}$	$<2.81 \times 10^{-16}$
Soft	$<8.32 \times 10^{-17}$	$<1.79 \times 10^{-16}$	$<1.66 \times 10^{-17}$	$<3.59 \times 10^{-17}$

TABLE 4
X-RAY PROPERTIES OF X-RAY DETECTED AGN

Source	z	X-ray Band	Γ^a	Flux ($\text{erg s}^{-1} \text{cm}^{-2}$)	Hard/Soft Flux Ratio	N_{H} (cm^{-2})	Abs. Corrected log L_x (erg s^{-1})	q'_{corr}
VLA J123556+621555	0.44	Full	1.37	1.31×10^{-14}	2.4	1.0×10^{22}	43.1	5.0
		Hard		9.10×10^{-15}			42.8	
		Soft		3.62×10^{-15}			42.8	
VLA J123640+621833	1.14	Full	>0.26	2.13×10^{-16}	<8.3	< 1.3×10^{23}	<42.5	>7.2
		Hard		$<2.76 \times 10^{-16}$			<42.4	
		Soft		3.20×10^{-17}			<42.4	
VLA J123642+621331	...	Full	1.35	2.76×10^{-16}	2.5	$(1.2 \times 10^{22} - 1.1 \times 10^{23})$	(41.6-43.3)	7.5- 7.4
		Hard		2.08×10^{-16}			(41.3-43.0)	
		Soft		8.03×10^{-17}			(41.3-43.0)	
VLA J123644+621133	1.01	Full	>1.43	2.44×10^{-16}	<2.2	< 2.0×10^{22}	<42.3	>7.8
		Hard		$<1.80 \times 10^{-16}$			<42.0	
		Soft		7.74×10^{-17}			<42.0	
VLA J123646+621404	0.96	Full	0.67	2.46×10^{-14}	6.4	7.6×10^{22}	44.3	4.7
		Hard		2.17×10^{-14}			44.1	
		Soft		3.26×10^{-15}			44.0	
VLA J123652+621444	0.32	Full	2.10	4.63×10^{-16}	0.9	...	41.2	6.8
		Hard		2.19×10^{-16}			40.8	
		Soft		2.44×10^{-16}			40.9	
VLA J123659+621832	...	Full	0.67	8.76×10^{-16}	6.5	$(3.9 \times 10^{22} - 4.3 \times 10^{23})$	(42.2-44.0)	6.8-6.4
		Hard		7.86×10^{-16}			(41.9-43.7)	
		Soft		1.18×10^{-16}			(41.9-43.7)	
VLA J123701+622109	0.8	Full	>0.40	3.22×10^{-16}	<7.1	< 6.8×10^{22}	<42.3	>7.0
		Hard		$<4.83 \times 10^{-16}$			<42.2	
		Soft		6.56×10^{-17}			<42.2	
VLA J123709+622258	1.23	Full	-0.58	5.21×10^{-15}	36.2	3.7×10^{23}	44.1	6.0
		Hard		4.99×10^{-15}			43.8	
		Soft		1.35×10^{-16}			43.8	
VLA J123713+621826	...	Full	1.37	1.69×10^{-15}	2.4	$(1.1 \times 10^{22} - 1.1 \times 10^{23})$	(42.4-44.1)	6.8-6.8
		Hard		1.19×10^{-15}			(42.1-43.8)	
		Soft		4.71×10^{-16}			(42.1-43.8)	
VLA J123721+621130	1.3	Full	0.28	5.09×10^{-16}	10.8	1.9×10^{23}	43.1	6.5
		Hard		5.07×10^{-16}			42.8	
		Soft		4.45×10^{-17}			42.8	

^aAlexander et al. assume a Γ of 1.4 for sources not detected in the hard band. For those AGN with hard band upper limits, however, we give the limit on Γ as calculated from the hard to soft band count rate ratio, H/S .